

Transport properties and equation of state of 1-bar eutectic melt in the system CaAl₂Si₂O₈-CaMgSi₂O₆ by molecular dynamics simulation

G. BEN MARTIN,^{1,*} MARK GHIORSO,² AND FRANK J. SPERA¹

¹Department of Earth Science, University of California-Santa Barbara, Webb Hall 1006-MC 9630, Santa Barbara, California 93106, U.S.A.

²OFM Research-West, 7336 24th Ave NE, Seattle, Washington 98115, U.S.A.

ABSTRACT

Empirical potential molecular dynamics (EPMD) simulations of 1-bar eutectic composition liquid in the system CaAl₂Si₂O₈-CaMgSi₂O₆ have been conducted using the interatomic pair-potential of Matsui (1998). Simulations using ~10 000 atoms over a wide range of conditions (ρ : 2200–5000 kg/m³; T : 1600–5500 K; P : 0–170 GPa) were used to derive an equation of state, determine self-diffusivities for all atoms, calculate melt viscosity, and investigate melt structures by coordination statistics. EOS results compare well to laboratory shock wave data up to ~25 GPa, diverging at higher pressure. Based on simulations of the end-member compositions of the join using the same potential, non-ideality in the volume of mixing at pressures below 10 GPa disappears at higher pressures. Ideal volume mixing at elevated pressure is consistent with inferences from laboratory shock wave studies of liquids in this system. The non-ideal volume of mixing at low pressure is directly correlated to structural differences between the end-member liquids and the mixing of cation-anion coordination polyhedra of differing volume. Self-diffusivities show reasonable agreement with laboratory values, with activation energies and activation volumes in the range 90–100 kJ/mol and 1–3 cm³/mol, respectively. Shear viscosities at 3500 K span from 1.8×10^{-3} Pa·s at low P to $\sim 4.4 \times 10^{-3}$ Pa·s at ~14 GPa.

Keywords: Anorthite, diopside, eutectic, high pressure, transport, structure, equation of state, diffusion, viscosity, volume mixing, basalt

INTRODUCTION

Liquid of 1-bar (10⁻⁴ GPa) eutectic composition in the system CaAl₂Si₂O₈-CaMgSi₂O₆ serves as a compositional analog for basaltic liquid, the most common magma on Earth, terrestrial planets, and parent bodies of achondritic meteorites. Understanding the pressure (P) and temperature (T) dependence of self-diffusivities, the shear viscosity, and equation of state (EOS) of basaltic liquid is relevant to myriad problems related to planetary differentiation and magma transport phenomena. Laboratory experiments over the wide range of P - T conditions pertinent to the Earth's mantle and the interiors of recently discovered super-Earth's (Udry et al. 2007) are expensive, time consuming, and difficult to carry out. Molecular dynamics (MD) simulation is a useful tool for the investigation of molten geoliquids, as demonstrated in numerous studies within the past decade using both first-principles (FPMD) (e.g., Stixrude and Karki 2005; Wan et al. 2007; Guillot and Sator 2007; de Koker et al. 2008; Vuilleumier et al. 2009; Karki and Stixrude 2010) and empirical potential molecular dynamics (EPMD) (e.g., Lacks et al. 2007; Ghiorso et al. 2009; Spera et al. 2009, 2011; Ghiorso and Spera 2009).

In this study, we report the results of EPMD simulations on liquid of 1-bar eutectic composition in the system CaAl₂Si₂O₈-CaMgSi₂O₆ (An₃₆Di₆₄ by molar abundance) up to 170 GPa and 5500 K using the pair potential of Matsui (1998) and compare with available experimental data to deduce the limit of validity of the Matsui potential. Melt structure and properties are determined

at 118 state points, most of which lie in the equilibrium liquid field, and results are used to derive an equation of state (EOS) for the equilibrium liquid following the methods outlined in Ghiorso et al. (2009). Self-diffusivities of Ca, Mg, Al, Si, and O are calculated at each state point, and long duration simulations of ~5 nanoseconds (ns) are used to determine the shear viscosity based on the time decay of the correlation of appropriate components of the stress tensor. Resulting values for diffusion and shear viscosity are fit to Arrhenian expressions to obtain values for the activation energy and activation volume for self-diffusion and viscous flow. Liquid properties are compared to laboratory values and other computational studies and related to melt structures determined by nearest-neighbor coordination statistics. We find that the EOS based on the transferable potential of Matsui (1998) is a useful liquid model up to ~25 GPa; however, at higher pressure, the Matsui-derived EOS deviates from shock wave data. The thermodynamic and transport model for eutectic composition liquid developed in this study is useful for temperatures in the range 2000–5000 K and pressures up to ~25 GPa. Additional MD simulations, preferably by first-principles methods (FPMD) or with a more suitable EPMD pair-potential valid to high pressures, are needed to extend the EOS to greater pressure.

METHODS

EPMD simulations were carried out in the microcanonical (NEV) ensemble (constant N , E , and V) using the transferable pair potential model of Matsui (1998) for the CaO-MgO-Al₂O₃-SiO₂ (CMAS) system. A detailed description of the numerical methods and implementation of the MD simulations may be found elsewhere (e.g., Spera et al. 2009; Ghiorso et al. 2009). Each simulation volume

* E-mail: gbenmartin@umail.ucsb.edu

contained 9995 atoms corresponding to a mixture of 42 wt% $\text{CaAl}_2\text{Si}_2\text{O}_8$ and 58 wt% $\text{CaMgSi}_2\text{O}_6$ (the 1-bar eutectic composition), approximating a basaltic liquid composition. In molar terms, the eutectic composition melt is 36 mol% $\text{CaMgSi}_2\text{O}_6$ and 64 mol% $\text{CaAl}_2\text{Si}_2\text{O}_8$. Simulations of 50 picoseconds (ps) were used to develop the equation of state (EOS) data and to compute self-diffusivities. The shear viscosity was found using longer simulations, up to 5 nanoseconds (ns). The time step was 1 femtosecond (fs). One hundred and eighteen simulations were carried out along 20 isochors spanning the density interval 1900–5500 kg/m³. Simulation pressure and temperature range over 0–172 GPa and 1750–5550 K, respectively. A large portion of these data, specifically all ergodic simulations, were used to develop an internally consistent EOS for the liquid following the methods outlined by Ghiors et al. (2009).

Self-diffusivity was calculated using the Einstein relation based on the mean-squared displacement (MSD) of each atom in 50 ps using appropriate time averaging over all atoms (Rapaport 1995). The MSD is the bracketed term in the expression

$$D = \frac{1}{6N_\alpha t} \left\langle \sum_{j=1}^{N_\alpha} [r_j(t) - r_j(0)]^2 \right\rangle \quad (1)$$

where r_j is the position of the j^{th} atom of species α at time t after the origin time. Self-diffusivities were determined for the entire P - T range, which encompasses both the equilibrium liquid state and the glass.

Shear viscosity was calculated in the P - T range of 0.2–16 GPa and 1850–4100 K. All elements of the pressure tensor were recorded at each timestep for the computation of shear viscosity (η) using the Green-Kubo (linear response) relations. This involves integration and averaging of the autocorrelation function for the five independent components of the stress tensor. There are three off-diagonal components of the stress tensor each of the form

$$\eta = \frac{V}{kT} \int_0^\infty \left\langle \sum_{x < y} P_{xy}(t) P_{xy}(0) \right\rangle dt \quad (2)$$

where V is the volume of the system, k is Boltzmann constant, and P_{xy} is, for example, the xy component of the stress. In addition to the off-diagonal stress terms, there are two additional independent stress components, $\frac{1}{2}(P_{xx} - P_{yy})$ and $\frac{1}{2}(P_{xx} - P_{zz})$, also used in the calculation of shear viscosity. The reported viscosity is the average of all five independent estimates; the quoted precision is the standard deviation of the five estimates. Details on the implementation of the Green-Kubo scheme for shear viscosity from molecular dynamics simulation results may be found in Nevens and Spera (2007).

Melt structure was investigated by analysis of nearest-neighbor coordination statistics between each atom pair based on the radial distribution function (RDF). A pair radius was defined as the first minimum after the first maximum in the RDF for the pair, and the coordination number of each species pair was computed by counting the number of atoms of a chosen species around each atom of the same or different species within this pair radius and averaging this number over space and time.

RESULTS

EOS and thermodynamics

All 118 thermodynamic state points simulated are shown in Figure 1 in pressure-temperature coordinates. Results are collected for each simulation in the electronic appendix¹, including the mean temperature (T), its fluctuation (σ_T), mean pressure (P), its fluctuation (σ_P), internal energy (E), kinetic energy (E_K), potential energy (E_P), and self-diffusivity for Ca, Mg, Al, Si, and O. Typical fluctuations in T and P are $\sigma_T \approx 25$ K and $\sigma_P \approx 0.3$ GPa, respectively, which reflects the relatively large number of atoms used in the simulations ($N \approx 10,000$).

To construct the equation of state (EOS) and transport properties of the equilibrium (ergodic) liquid, the simulations have been filtered to exclude non-ergodic simulations. Our interests in this study lie in the properties of the equilibrium or metastable liquid, not thermally arrested material (glass). A glass, or arrested liquid, is a nonequilibrium phase with properties that depend upon cooling rates during quenching and does not define the thermodynamic properties of the equilibrium liquid. As glass-forming materials are cooled, the sharply increasing viscosity of the liquid is accompanied by equally dramatic changes in the motion of tracer particles (i.e., self-diffusion) within the material. Perhaps the most fundamental way to identify non-Gaussian behavior and the breaking of ergodicity at the liquid to glass transition is to note the deviation of the logarithmic mean square displacement (MSD) from linear dependence on the logarithm of time. A detailed study of the dynamics and thermodynamics of the ergodic (liquid) to non-ergodic (glassy) transition for a typical geoliquid, the aluminosilicate $\text{CaAl}_2\text{Si}_2\text{O}_8$, has been presented elsewhere (Morgan and Spera 2001). In the anomalous non-ergodic region, the mean square displacement (MSD) (see Eq. 1)

$$\text{MSD} = \{[r(t) - (0)]^2\} = 6D_\alpha t^\alpha \quad (3)$$

exhibits power-law behavior. That is, the exponent α in Equation 3 is not equal to unity as in classical Gaussian diffusion based on the Einstein random walk. Instead, an anomalous regime called subdiffusion with $\alpha < 1$ is encountered for the ensemble (Metzler and Klafter 2004; Weeks and Weitz 2002 and references therein). Typically, subdiffusion arises when a system possesses memory. By studying temporal correlations in particle motions, subdiffusion has been shown to be due to the “cage effect;” an atom alternates between being trapped in a local cage of adjoining atoms and jumping to a new location when the cage rearranges. The size and lifetime of a cage is related to the Adam-Gibbs concept of cooperatively rearranging regions (CRR) within the glass (Morgan and Spera 2001; Stevenson et al. 2006). Consequently, our method of separating

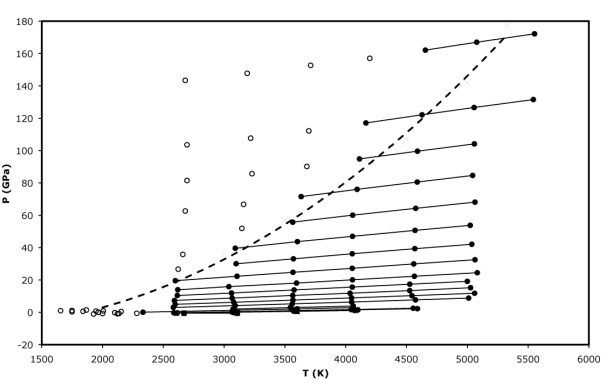


FIGURE 1. Pressure-temperature results of all state points simulated. Filled circles represent state points used for the derivation of the equation of state (EOS), while open circles represent those that were not included to ensure ergodicity. Solid lines represent isochors calculated from the EOS. The dashed curve represents the locus of P vs. T where the calculated self-diffusion is constant, at $10^{-9} \text{ m}^2/\text{s}$.

¹ Deposit item AM-12-046, Electronic annex-1 (EA-1). Deposit items are available two ways: For a paper copy contact the Business Office of the Mineralogical Society of America (see inside front cover of recent issue) for price information. For an electronic copy visit the MSA web site at <http://www.minsocam.org>, go to the *American Mineralogist* Contents, find the table of contents for the specific volume/issue wanted, and then click on the deposit link there.

ergodic from non-ergodic state points is to examine log MSD vs. log t plots for each state point and determine by linear regression the slope α . For state points exhibiting ergodicity, α is essentially equal to unity and deviates from unity by <1%, generally. Minor deviation represents statistical uncertainty of the regression. On the other hand, for simulations run at conditions within the glass field, α deviates from unity by 20–30% over the course of a 50 ps simulation and is readily apparent without ambiguity. The state points used for the EOS derivation are depicted in Figure 1 as filled circles and those excluded are depicted as empty circles. Filtering the primary data set of 118 simulations by this method produces a subset of 86 state points that have been used to calibrate the EOS.

Computed values of the specific potential energy, E_p , vs. $T^{3/5}$ are shown in Figure 2. The observed linear relationships along any given isochor verify the scaling relations of Rosenfeld and Tarazona (1998; hereafter RT98), who propose the relation

$$E_p = a(V) + b(V)T^{3/5} \quad (4)$$

where $a(V)$ and $b(V)$ are unspecified functions of volume (V) for fully ergodic liquids. Physically, $a(V)$ is the Helmholtz free energy at 0 K. Adherence to RT98 scaling has been demonstrated for molten SiO_2 (Saika-Voivod et al. 2000), Mg_2SiO_4 (Martin et al. 2009), $\text{CaAl}_2\text{Si}_2\text{O}_8$ (Ghiorso et al. 2009), and MgSiO_3 (Spera et al. 2011) based on empirical potential molecular dynamics (EPMD) and for the first-principles simulations (FPMD) of Stixrude and Karki (2005) for liquid MgSiO_3 and of de Koker (2010) for liquid $\text{CaAl}_2\text{Si}_2\text{O}_8$. Not surprisingly, state points identified as glassy by the MSD method exhibited deviations from the linear RT98 scaling relation of E_p vs. $T^{3/5}$ by more than two standard deviations of the fit. In contrast, the filtered MD simulations satisfy Equation 4 along a given isochor to a precision equivalent to the computed simulation temperature fluctuation σ_T . Slopes and intercepts of the scaling relations are reported in Table 1, all of which have an R^2 in the range of 0.9978–0.9999. The functions $a(V)$ and $b(V)$ can be fitted from the linear parameterizations in Table 1 by following techniques

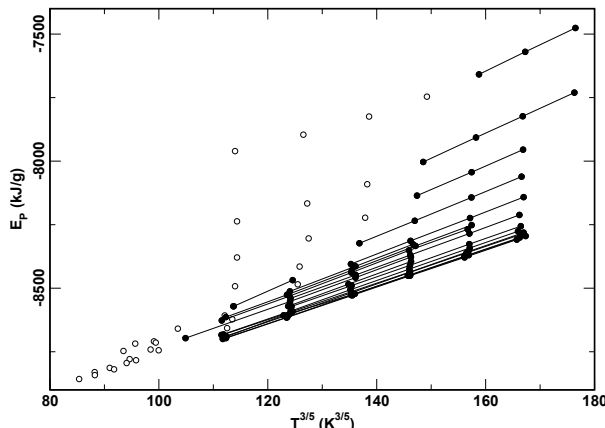


FIGURE 2. Rosenfeld and Tarazona (1998) scaling of potential energy-temperature relations of An-Di eutectic liquid. Solid symbols refer to state points from a data set filtered to ensure temperatures above the glass transition (see text and Table 2).

TABLE 1. Rosenfeld-Tarazona scaling ($U = a + bT^{3/5}$)

ρ (g/cm ³)	b [kJ/(g – K ^{3/5})]	a (kJ/g)
1.900	0.03629	-40.00
2.148	0.03397	-39.86
2.200	0.03372	-39.87
2.250	0.03348	-39.87
2.397	0.03225	-39.81
2.700	0.03144	-39.88
2.850	0.03101	-39.87
3.000	0.03067	-39.86
3.150	0.03039	-39.84
3.300	0.02990	-39.75
3.500	0.03049	-39.78
3.700	0.03144	-39.81
3.900	0.03269	-39.83
4.100	0.03474	-39.90
4.300	0.03687	-39.91
4.700	0.04111	-39.62
5.000	0.04320	-38.93

TABLE 2. Coefficients for Rosenfeld-Tarazona polynomial functions

	$a(V) = \sum_{i=0}^6 c_i v^i$	$b(V) = \sum_{i=0}^6 c_i v^i$
c_0	389.126	-1.31565
c_1	-7589.50	28.0118
c_2	55084.6	-227.487
c_3	-209870	940.497
c_4	442631	-2110.25
c_5	-490001	2452.87
c_6	222471	-1158.75

outlined in Ghiorso et al. (2009). Polynomial functions in specific volume are developed from these parameterizations and are reported in Table 2.

In Figure 3, the p - P coordinates of all state points studied by MD simulation are shown. As described in Martin et al. (2009) and Ghiorso et al. (2009), an equation of state and complete thermodynamic model for An-Di eutectic liquid can be developed from these data by utilizing the RT98 scaling functions of Table 2 and a parameterization of V - P relations along a reference isotherm. Following our previous work, we employ the Universal EOS (Vinet et al. 1986) for the reference isotherm. The three parameters of this EOS, V_0 , K , and K' are the zero pressure volume, isothermal bulk modulus, and the pressure derivative of the isothermal bulk modulus for reference temperature T_o . Selecting the nominal 3500 K isotherm, Universal EOS parameters are optimized from the data array, yielding $V_0 = 0.693$, $K = 0.315$, and $K' = 11.44$. A temperature-dependent equation of state (hereafter, the RTU EOS),

$$P(V, T) = \left(\frac{T}{T_o} - 1 \right) \frac{da(V)}{dV} + \frac{5}{2} T^{3/5} \left[\left(\frac{T}{T_o} \right)^{2/5} - 1 \right] \frac{db(V)}{dV} + \frac{T}{T_o} \frac{3K(1-x)e^{\frac{3}{2}(K'-1)(1-x)}}{x^2}, \quad x = \left(\frac{V}{V_0} \right)^{1/3} \quad (5)$$

is constructed from the reference Universal EOS and Equation 4, following the procedure of Ghiorso et al. (2009). From the RTU EOS, all derivative and integral thermodynamic properties may be evaluated. The smooth curves plotted in Figure 3 are model predictions and illustrate the excellent applicability of

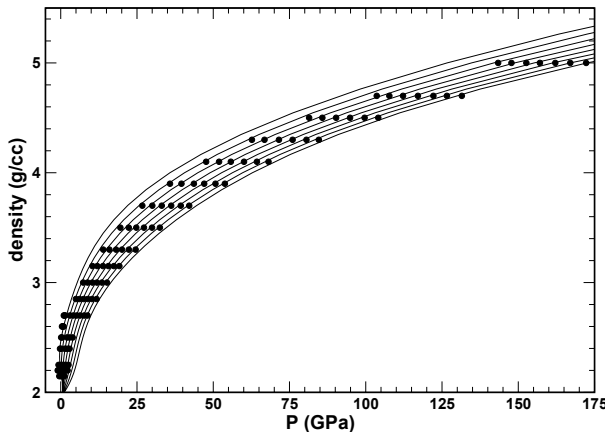


FIGURE 3. Density-pressure relations of An-Di eutectic liquid derived from the Matsui (1998) potential (solid symbols) and the RTU EOS (curves). Isotherms (500 K intervals) span the range 2000 K (uppermost curve) to 5500 K (lowermost curve).

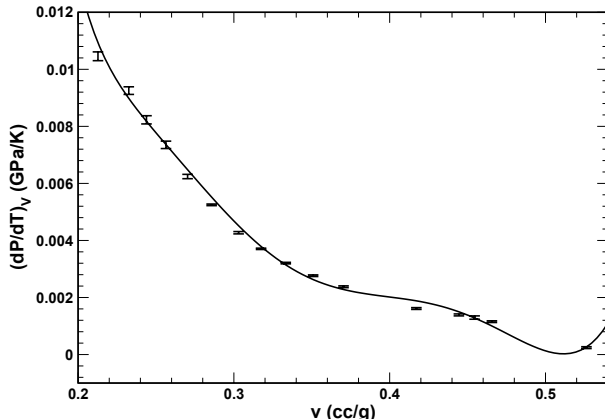


FIGURE 4. Variation of the thermal pressure coefficient with inverse density. Values derived from the MD state point array shown with uncertainties. The curve is calculated from the RTU EOS.

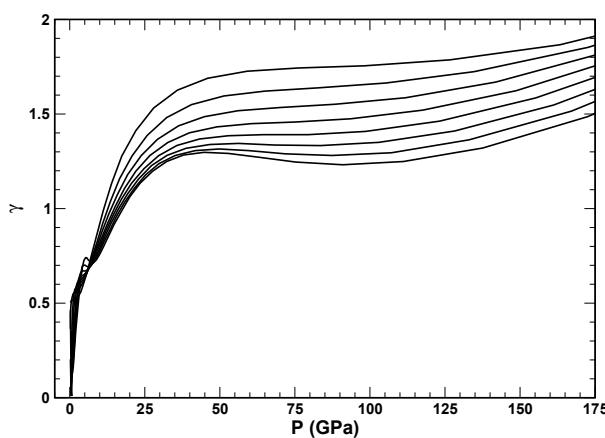


FIGURE 5. The thermal Grüneisen parameter calculated from the RTU EOS. Isotherms are shown spaced at 500 K intervals; uppermost curve is at 2000 K; lowermost curve is at 5500 K.

the RTU EOS formalism to the MD state point arrays.

In Figure 4, estimates of the thermal pressure coefficient obtained by finite differencing state points along isochors are plotted and compared to smoothed model estimates given as the continuous curves on Figure 4. The RTU EOS evidently provides an excellent representation across the wide P - T range of the simulations.

In Figure 5, the pressure variation of the thermal Grüneisen parameter, γ , is given, which varies from ~ 0.25 at zero pressure to a constant value of ~ 1.5 at high-pressure. It is significant that the thermal Grüneisen parameter displays a rather weak dependence on temperature below pressures of ~ 25 GPa. Even for greater pressures, the T dependence remains small.

Finally, in Figure 6 we have superimposed the liquid isentrope on phase relations of the CMAS system from Presnall et al. (2002). The isentrope was chosen to intersect the experimental solidus at 3 GPa. The difference in temperature between the zero pressure solidus and the extension of the eutectic liquid isentrope is about 240 K. This implies an available enthalpy of ~ 265 kJ/kg for partial melting, given an isobaric heat capacity of 1100 J/(kg·K), and roughly corresponds to $\sim 40\%$ melting of a model CMAS peridotite upon isentropic (reversible and adiabatic) decompression. A steeper adiabat in P - T coordinates would imply less partial melting.

The shock wave Hugoniot of An-Di eutectic liquid has been recently reevaluated and extended to higher pressure by Asimow and Ahrens (2010). Their data are plotted with uncertainty estimates in Figure 7 along with isotherms and a Hugoniot curve calculated from the EOS developed above [the method for Hugoniot curve calculation from an RTU EOS is given in Ghiorso et al. (2009)]. Agreement between the calculated Hugoniot and measured values is good at pressures below ~ 25 GPa, but breaks down at higher pressure. This discrepancy is largely due to the energy balance term in the Hugoniot cal-

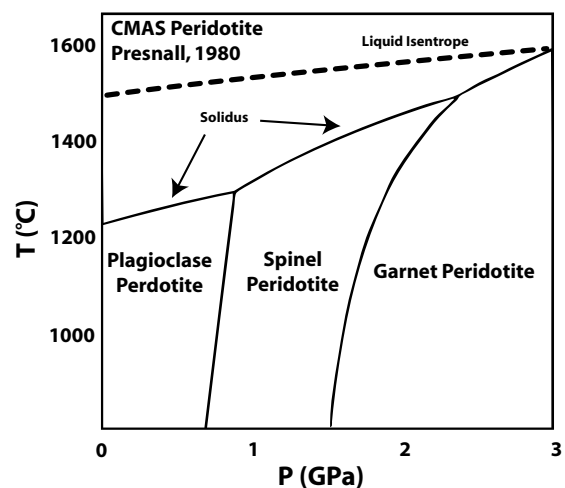


FIGURE 6. Isentrope of the liquid eutectic composition chosen to intersect the solidus of the laboratory results of Presnall et al. (2002) model at 3 GPa. The extent of partial melting of a peridotite in CMAS undergoing isentropic decompression is related to the difference in temperatures between the 1-bar solidus and the projection of the liquid adiabat to 1 bar.

culation, which drives implied shock temperatures to very high values at elevated pressure. Without considering the energy balance, the RTU EOS curves by themselves require temperature variation along the Hugoniot to be minimal, corresponding roughly to that displayed by an isentrope whose origin is the zero pressure melting point (Fig. 7). MD simulations of anorthite liquid (Ghiorso et al. 2009) and diopside liquid (Creamer et al. unpublished manuscript) calculated on the basis of the Matsui (1998) pair potential show an identical problem with their RTU EOS Hugoniots. These collective observations lead us to conclude that the EOS isotherms in Figure 7 should be displaced to higher densities at higher pressure. In other words, the pair-potential of Matsui underestimates the density of molten anorthite, diopside, and An-Di eutectic liquid at pressures above ~25 GPa. The measured Hugoniot points should fall along high-temperature EOS isotherms at elevated pressure. The application of the Matsui (1998) potential for eutectic An-Di liquid at pressures above ~25 GPa (within transition zone on Earth) cannot be recommended.

Coordination statistics

Nearest neighbor coordination statistics for all atoms at all state points were collected and examined. Here we discuss a subset of these, specifically coordination of O around Si, Al, Mg, Ca, and O and the coordination of Si, Al, Mg, and Ca around O at 3000 and 5000 K. Although structures are influenced by temperature at fixed pressure mainly by increasing nearest neighbor distances (e.g., bond lengths), the most important variable by far governing liquid structure is pressure (or volume). The notation AB^[n] is used to describe coordination polyhedra. In this notation, A refers to the central atom, B refers to the atom that is coordinated around A, and n gives the number of nearest neighbors of B surrounding the central A atom. The average coordination number (CN) of B around A is written with an overbar, \overline{CN} .

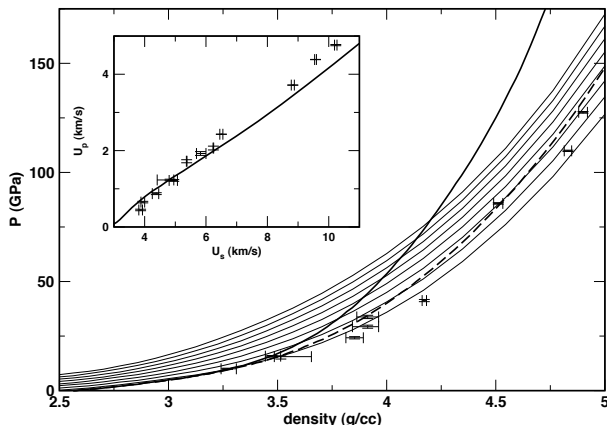


FIGURE 7. Calculations and data pertaining to the shock wave Hugoniot of An-Di eutectic liquid. Data points are from Asimow and Ahrens (2010), with uncertainties indicated. Dashed curves denote the RTU EOS Hugoniot. The solid bold curve in the main figure is an isentrope with origin at the zero pressure melting point. Solid thin curves denote isotherms of the RTU EOS, spaced at 500 K intervals, with the uppermost curve at 5500 K and the lowermost curve at 2000 K. In the inset, U_p refers to the particle velocity and U_s the velocity of the shock.

Oxygen around Si, Al, Mg, Ca, and O at 3000 K

In Figure 8a, the statistics of O around Si at 3000 K are portrayed. At low pressure, coordination of O around Si is dominated (>90%) by Si in tetrahedral coordination with oxygen (i.e., $\text{SiO}^{[4]}$ is the most common Si-O polyhedron), about 5% of the Si is pentahedrally coordinated by oxygen, and there is virtually no Si octahedrally coordinated. These features change rapidly as P increases such that by ~30 GPa the abundance of $\text{SiO}^{[4]}$ and $\text{SiO}^{[6]}$ are roughly equal (~25%) and $\text{SiO}^{[5]}$ attains a maximum abundance of ~50%. At $P > 40$ GPa, both tetrahedral and pentahedral Si decrease and octahedral Si becomes the most abundant coordination state. At the highest P studied, the melt is substantially an octahedral fluid with ~80% $\text{SiO}^{[6]}$, 10% $\text{SiO}^{[5]}$, and lesser amounts of $\text{SiO}^{[7]}$ and $\text{SiO}^{[8]}$.

Figure 8b shows the abundances of the various $\text{AlO}^{[n]}$ coordination polyhedra. The pattern is broadly similar to that of O around Si, provided a translation or “pressure shift” to lower pressure by ~15 GPa is made to the O around Si abundance pattern. For example, pentahedrally coordinated Al peaks at 18 GPa, vs. 30 GPa for pentaredrally coordinated Si. Also, $\text{AlO}^{[6]}$ reaches 50% at 32 GPa, whereas octahedrally coordinated Si reaches 50% abundance at ~45 GPa. An important difference in Al and Si coordination by oxygen is that, unlike the case for Si, a substantial amount of Al is in the $\text{AlO}^{[7]}$ state at the highest P studied (~30% $\text{AlO}^{[7]}$ at 140 GPa). Based on the larger size of Al vs. Si, this feature is expected.

The coordination of O around Mg is depicted in Figure 8c. At low P , about equal amounts of $\text{MgO}^{[4]}$, $\text{MgO}^{[5]}$, and $\text{MgO}^{[6]}$ are present. As P increases, tetrahedral and pentahedral Mg both decrease, whereas octahedral Mg increases to a maximum concentration at ~15 GPa. Abundances of $\text{MgO}^{[7]}$, $\text{MgO}^{[8]}$, and $\text{MgO}^{[9]}$ increase monotonically. \overline{CN} increases from ~5 at 1 bar to ~7.5 at 70 GPa. Note that above ~80 GPa there is no significant change in the mean coordination number of O around Mg (i.e., for polyhedra $\text{MgO}^{[n]}$, n is constant). We interpret this transition from “unfrozen” to “frozen” statistics indicative of close approach of the computer glass transition, at 3000 K and ~70 GPa. In other words, on the timescale of the simulations there is a transition from ergodic to non-ergodic behavior because the metastable liquid has become a computer glass with a frozen structure. This effect is most notable in coordination statistics for Mg compared to the other atoms because the self-diffusivity of Mg is greater than for any other atoms in eutectic liquid and hence the ergodic to non-ergodic transition is most marked (see “Self-diffusion” section below).

Coordination statistics for O around Ca are given in Figure 8d. At 1 bar, \overline{CN} is ~7 and increases asymptotically to ~10 at ~80 GPa. $\text{CaO}^{[8]}$ and $\text{CaO}^{[9]}$ peak at 7 and 18 GPa, respectively, monotonically decreasing at higher pressure, whereas the higher coordination polyhedra such as $\text{CaO}^{[10]}$ and $\text{CaO}^{[11]}$ increase from low P and become approximately constant for $P > 70$ GPa, at the dynamical transition from liquid to glass.

Finally, we can examine O around O statistics in Figure 8e. At low P , the mean coordination number of O around O is ~9.9, which rapidly increases to ~12 at 55 GPa. At higher P , the mean CN decreases and eventually becomes constant at the computer glass transition. In detail, $\text{OO}^{[10]}$, $\text{OO}^{[11]}$, $\text{OO}^{[12]}$, and $\text{OO}^{[13]}$ each

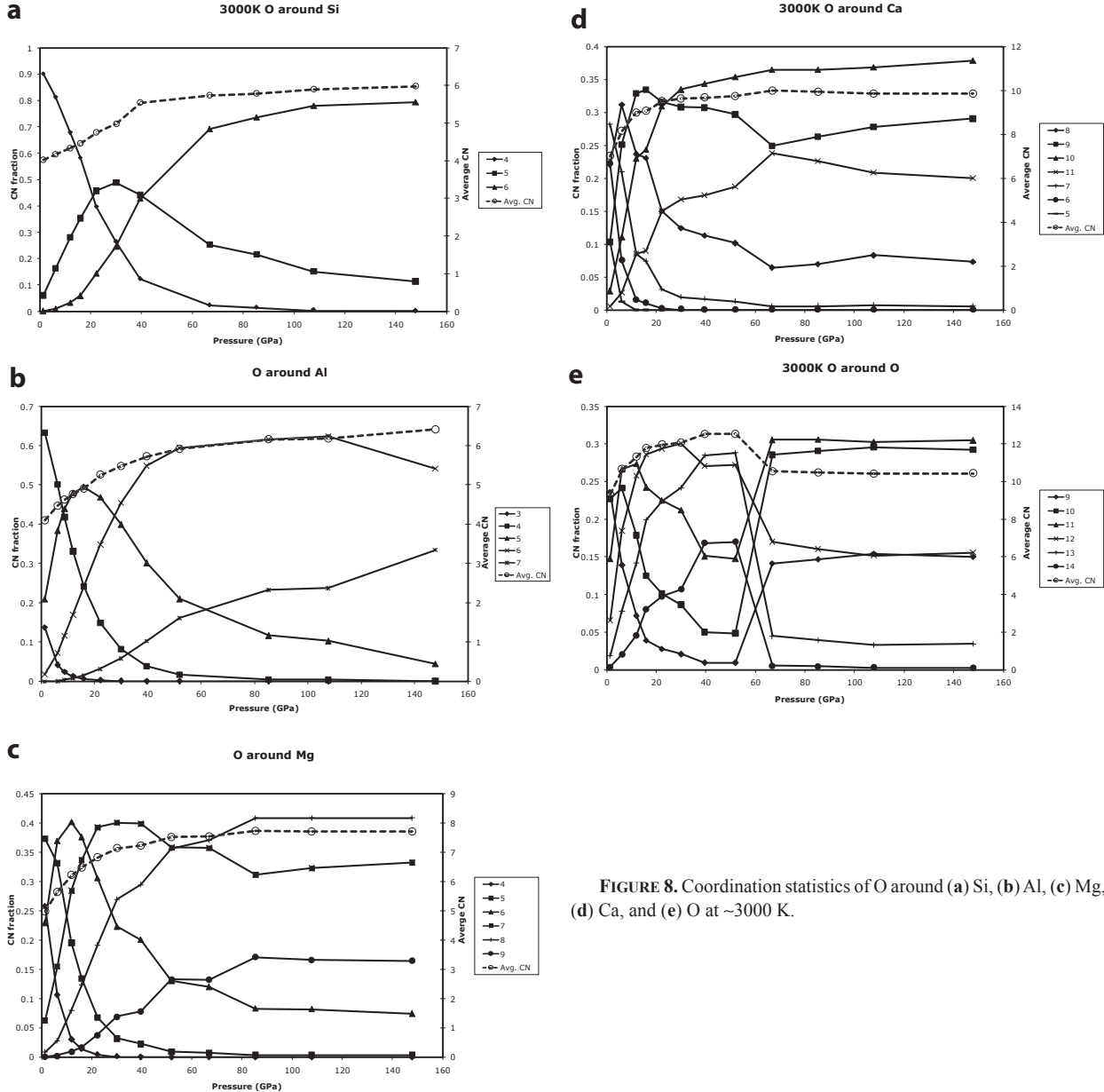


FIGURE 8. Coordination statistics of O around (a) Si, (b) Al, (c) Mg, (d) Ca, and (e) O at ~3000 K.

attain maxima at successively higher P . The decrease in \overline{CN} around 60 GPa is similar to a comparable decrease in liquid $MgSiO_3$ (Spera et al. 2011). Again, at ~70 GPa the statistics appear “frozen” as the computer glass transition is approached.

Si, Al, Mg, and Ca around O at 3000 K

Coordination statistics for Si around O are presented in Figure 9a. At 1 bar, $OSi^{[0]}$, $OSi^{[1]}$, and $OSi^{[2]}$ constitute 12, 58, and 30% of the Si around O speciation. These values can be contrasted with the 1-bar structure of anorthite and diopside. Anorthite has a fully polymerized structure—each O has two nearest neighbors of either Si or Al. In diopside, half of the O has two nearest neighbors of Si and half of the O has one, giving

$\overline{CN} \sim 1.5$. As P increases, melt polymerization increases. That is, O with one nearest Si neighbor decreases, and both $OSi^{[2]}$ and tricluster oxygen ($OSi^{[3]}$) increase. At ~75 GPa, Si around O statistics become frozen as the glass transition at 3000 K is approached. Unlike Si, Al behaves in eutectic liquid more like a network modifier than a network-former. In Figures 9b and 9c, coordination statistics for Al around O and Mg around O are presented. The similarities are quite evident. At low P , most (60%) of the oxygen have no nearest neighbor of Al (Mg) and about 30% have one nearest neighbor. Only about 5% of the O atoms are surrounded by two neighbors of Al (Mg), implying that although $AlO^{[4]}$ tetrahedra are abundant, they show very little tendency to polymerize with each other. In Figure 9d, the

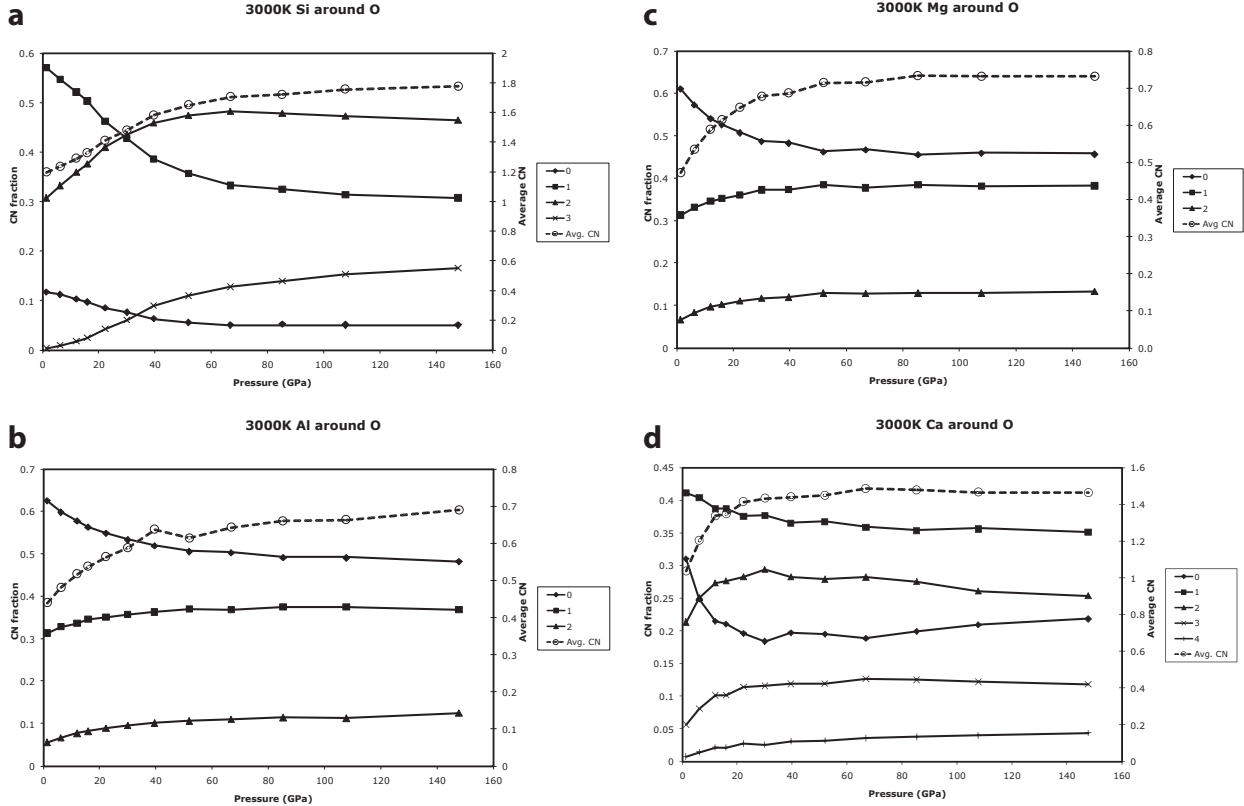


FIGURE 9. Coordination statistics of (a) Si, (b) Al, (c) Mg, and (d) Ca around O at ~3000 K.

statistics of Ca around O are given. The main effect of increasing P is to favor higher coordination numbers. $\text{OCa}^{[0]}$ and $\text{OCa}^{[1]}$ decrease while the fraction of $\text{OCa}^{[2]}$ and $\text{OCa}^{[3]}$ (tricluster O) increases. Once again, the approach to the glass transition is clearly seen at ~80 GPa where the statistics become “frozen.”

Coordination statistics at 5000 K

Coordination statistics for all atoms at 5000 K are quite similar to those at 3000 K, except that average coordination numbers are higher by ~10–15% at any given pressure compared to the statistics at 3000 K. These differences reflect the decrease in liquid density as T increases isobarically. Detailed examination of the statistics at 5000 K does reveal two important points. The first is that the computer glass transition at 5000 K is ~110 GPa based on the pressure at, which statistics become “frozen.” The second point is noted in Figure 10, which portrays the coordination of O around O, or the so-called “oxygen sublattice.” The average CN of O around O decreases in the pressure range 80–120 GPa from ~12.5 to ~10.5. This same effect has been noted in MgSiO_3 liquid using the Matsui potential and, significantly, an independent potential applicable to MgSiO_3 developed by Oganov et al. (2000). The fact that two distinct potentials give rise to this phenomenon lends credence to the surprising finding that there is a decrease in the average coordination number for O around O as pressure increases. This result is discussed in more detail elsewhere (Spera et al. 2011).

Self-diffusion

Diffusivities were calculated at each state point for all atoms using Equation 1 and are given in EA-1. These data were fitted by multiple linear regression models to a modified Arrhenius expression

$$D = D_0 \exp\left(\frac{-E_D + (v_{D_0} + v_{D_1}P)P}{RT}\right) \quad (6)$$

where E_D is the activation energy for diffusion, D_0 is the pre-exponential frequency factor, R is the universal gas constant, and the constants v_{D_0} and v_{D_1} give the variation of activation volume, v_D , with pressure, $v_D = (v_{D_0} + v_{D_1})P$. The results of the regression analysis given in Table 3 were determined using only ergodic simulations since we are interested in the self-diffusivities of atoms in the liquid, not the glass. Activation energies vary from ~76 kJ/mol (Ca and Mg) to 92–100 kJ/mol for Al, O, and Si, respectively. The zero-pressure activation volume for all atoms falls between a low of 1.3 cm³/mol for

TABLE 3. Parameters derived from multiple linear regression of diffusion data fit to Equation 11

Species	E_D (kJ/mol)	v_{D_0} (cm ³ /mol)	v_{D_1} [cm ³ /(mol·GPa)]	D_0 (m ² /s)
Al	92.34	1.31	-2.81E-03	3.39E-07
Ca	75.64	1.93	-5.48E-03	2.92E-07
Mg	76.87	1.51	-2.44E-03	3.45E-07
O	97.42	1.49	-3.21E-03	3.63E-07
Si	99.35	1.30	-2.71E-03	2.91E-07

Al and Si and a high of $1.9 \text{ cm}^3/\text{mol}$ for Ca, with O and Mg in between. These activation volumes are typical for molten silicates, both experimentally (Zhang et al. 2010) and in other MD studies (Karki et al. 2011).

Figure 11 shows calculated diffusivities along sample isotherms of 3000 and 5000 K for all species, using Equation 6 and the values from Table 3. Relative self-diffusion behavior between atom species with respect to pressure is the same for both temperature regimes. At low pressure, Mg is the most mobile atom, but this behavior is inverted approaching the highest pressures as it becomes the slowest. Oxygen, the only anion, remains one of the slowest diffusers across the whole P - T range. The largest constituent atom, Ca, is also relatively slow at intermediate and high pressures.

Shear viscosity

The shear viscosity was calculated for pressures spanning 0.2–16 GPa and temperature 1675–4100 K and are depicted in Figure 12. Multiple linear regression was used to fit the data to a modified Arrhenius equation, which is known to capture the shear viscosity of molten silicates at elevated temperature and pressure for MD fluids as well as experimental data. The modified Arrhenius expression is

$$\eta = \eta_0 \exp\left(\frac{E_\eta + (v_{\eta_0} + Pv_{\eta_1})P}{RT}\right) \quad (7)$$

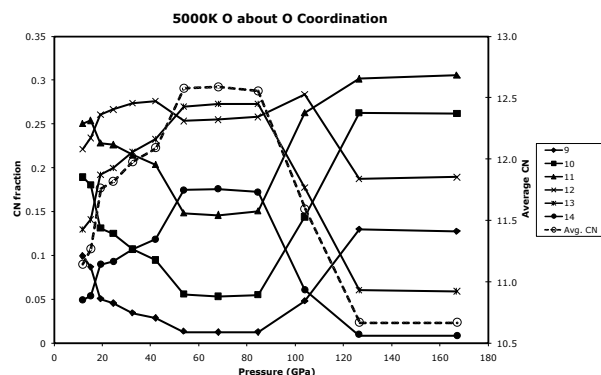


FIGURE 10. Coordination statistics of O around O at ~ 5000 K.

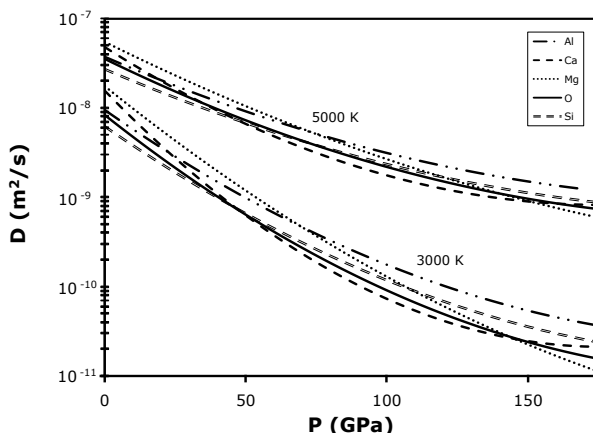


FIGURE 11. Self-diffusion of all species along the 3000 and 5000 K isotherms.

where E_η is the activation energy for viscous flow, the activation volume is a linear function of pressure, $v_\eta = v_{\eta_0} + Pv_{\eta_1}$, and R is the universal gas constant. The pre-exponential factor η_0 corresponds to the shear viscosity in the limit $T \rightarrow \infty$. The regression analysis gives $\eta_0 = 1.788 \times 10^{-4} \text{ Pa}\cdot\text{s}$, $E_\eta = 69 \text{ kJ/mol}$, $v_{\eta_0} = 2.66 \text{ cm}^3/\text{mol}$, and $v_{\eta_1} = -0.0537 \text{ cm}^3/\text{mol}\cdot\text{GPa}$. The correlation coefficient of the fit is $R^2 = 0.987$.

DISCUSSION

The values for viscosity calculated here are greater than those calculated for Mg_2SiO_4 (Martin et al. 2009), but less than those calculated for MgSiO_3 (Nevins et al. 2009), as expected based on the extent of polymerization and substitution of Ca for Mg in $\text{CaMgSi}_2\text{O}_6$ relative to $\text{Mg}_2\text{Si}_2\text{O}_6$. Few viscosity values exist in the experimental literature for Mg_2SiO_4 eutectic liquid above 1 bar. Taniguchi (1992) reports 1923 K viscosities at 1.5 and 2 GPa of 0.44 and 0.52 Pa·s, respectively, whereas the model equation gives values about $20\times$ smaller—0.017 and 0.018 Pa·s. Note that the density was measured on the quenched glass and not the actual liquid. However, the linear dependence of the viscosity on the density means that even a 10–20% difference in density cannot account for the order of magnitude difference we observe.

Table 4 shows a comparison of zero pressure extrapolations at 2273 K of our diffusion values and those of other workers. All species' coefficients from this study are below those of the MD

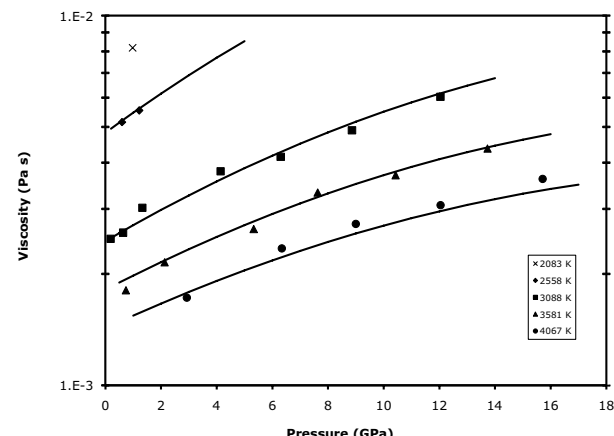


FIGURE 12. Shear viscosity of the An-Di liquid calculated from the Green-Kubo relation. Solid lines are drawn from a regression analysis of a modified Arrhenius equation (Eq. 12).

TABLE 4. Comparison of zero pressure extrapolations at 2273 K [D ($10^{-9} \text{ m}^2/\text{s}$)]

O	Si	Al	Mg	Ca
0.9	0.8	2.3	4.8	3.5
1.3*	0.9*	1.9*	5.6*	4.6*
0.4†	0.2‡	0.9	2.1#	1.7#
0.2‡	0.2§			3.1**
0.3§	0.45			0.6††

* Vuilleumier et al. (2009).

† Dunn (1982).

‡ Tinker et al. (2003).

§ O and Si in basalt by Lesher et al. (1996).

|| From the model of Mungall (2002) using viscosity data by Urbain et al. (1982).

Mg and Ca in haplobasalt by LaTourrette et al. (1996).

** Ca in basalt by Hofmann and Magaritz (1977).

†† Ca in basalt by Jambon and Carron (1978).

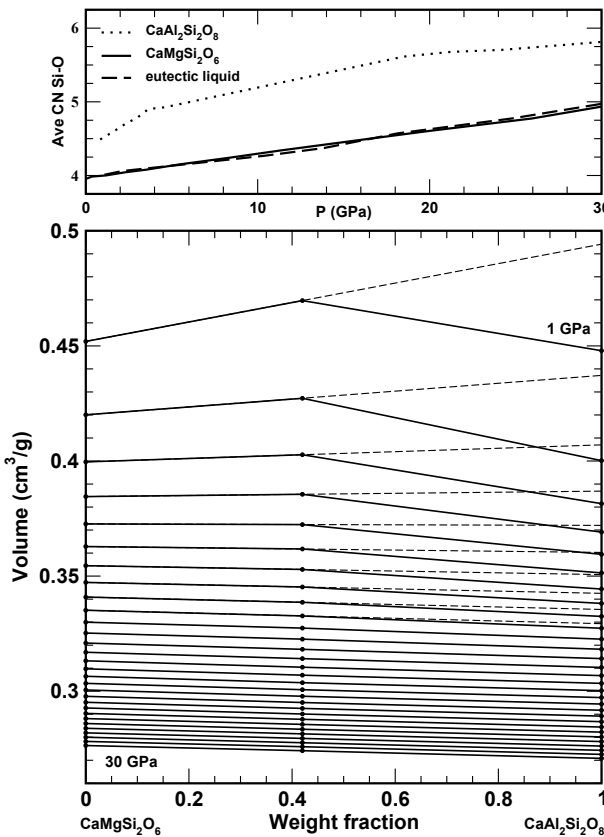


FIGURE 13. Specific volumes (**lower panel**) and average coordination statistics of O about Si (**upper panel**) for three liquids along the binary join $\text{CaAl}_2\text{Si}_2\text{O}_8$ - $\text{CaMgSi}_2\text{O}_6$. In the lower panel isobars are spaced at one GPa. Black lines connect values interpolated from EOS parameterizations of EPMD data. Dashed lines indicate extrapolations of linear mixing trends from pure $\text{CaMgSi}_2\text{O}_6$ liquid through the eutectic composition.

calculations of Vuilleumier et al. (2009) who used a different inter-atomic potential and reported values up to 2–3× higher than other experimental values. Tinker et al. (2003) calculated diffusion coefficients for Si and O for the eutectic composition, but their reported values are systematically an order of magnitude slower than those reported here at similar P and T . However, the two data sets have only a small overlap in P and T space, covering the low ranges of 0–2 GPa and 1800–2100 K. Still, the values presented here are within the variation of other studies in the literature.

As noted above, the filtered data used for the EOS analysis excluded state points that exhibited subdiffusion. These excluded state points deviate from the linear fit of the E_P vs. $T^{3/5}$ slope by more than $\pm 2\sigma$, which is expected since the linear relationship between molar potential energy and $T^{3/5}$ is strictly for ergodic liquids, not for a thermally arrested glass (Rosenfeld and Tarazona 1998). Heuristically, the excluded data roughly coincide with state points for which the self-diffusivity of oxygen, D_0 , is less than $\sim 10^{-9} \text{ m}^2/\text{s}$. The dashed line in Figure 1 defines the locus of points in P and T space where $D_0 = 10^{-9} \text{ m}^2/\text{s}$. This diffusion cut-off implies a root mean square travel distance for a typical oxygen of $\sim 3.2 \text{ \AA}$ in 50 ps. Because this

distance is roughly twice the mean O-Si separation, it is a conservative criterion that ensures ergodicity.

VOLUME MIXING OF LIQUIDS ALONG THE $\text{CaAl}_2\text{Si}_2\text{O}_8$ - $\text{CaMgSi}_2\text{O}_6$ JOIN

Using the EOS from the eutectic liquid of this study in combination with those obtained using the Matsui (1998) potential for anorthite liquid (Ghiorso et al. 2009) and diopside liquid (Creamer et al. in prep) we can investigate the volume of mixing of binary liquids across the $\text{CaAl}_2\text{Si}_2\text{O}_8$ - $\text{CaMgSi}_2\text{O}_6$ join. The lower panel of Figure 13 portrays computed liquid volume at 3500 K for pressures from 1 to 30 GPa. At pressures below 10 GPa, the volume of mixing is clearly non-ideal. At higher pressures, mixing is ideal within the uncertainties of the simulation (deviations from a linear fit are <0.2%).

The average CN of O about Si ($\text{SiO}^{[\text{avg}]}$) for the three liquids is plotted in the upper panel of Figure 13. $\text{SiO}^{[\text{avg}]}$ is strongly correlated to other structural features of the liquid, and the data plotted in Figure 13 demonstrate that, by this measure, diopside liquid and eutectic liquid have the same structure over the whole range of pressures. On the basis of structural similarity, we would expect ideal volume mixing between diopside and eutectic liquid. The figure shows this linear-mixing trend extrapolated to pure $\text{CaAl}_2\text{Si}_2\text{O}_8$ (the dashed lines), where the intercept can be interpreted as the volume of anorthite-liquid in the hypothetical structural state of diopside/eutectic liquid (i.e., this volume corresponds to anorthite liquid in the standard state structure of diopside/eutectic liquid). As Figure 13 shows, the volumes of all three liquids are consistent with ideal mixing above 10 GPa. From this observation, we can conclude that the structural differences in the liquids become irrelevant once the tetrahedra, pentahedra, and octahedra are compressed. By implication, $\text{MO}^{[4]}$, $\text{MO}^{[5]}$, and $\text{MO}^{[6]}$ polyhedra must all be about the same volume by ~ 10 GPa. This implies that the compressibility of $\text{SiO}^{[4]}$ must be larger than $\text{SiO}^{[5]}$, which in turn is larger than $\text{SiO}^{[6]}$ at low P , for all three polyhedra to acquire roughly the same volume when the liquid is compressed to 10 GPa. Our analysis of the mixing volumes along the $\text{CaAl}_2\text{Si}_2\text{O}_8$ - $\text{CaMgSi}_2\text{O}_6$ join is congruent with the shockwave EOS results of Rigden et al. (1989), and subsequently Asimow and Ahrens (2010), who also infer linear mixing of volume in the $\text{CaAl}_2\text{Si}_2\text{O}_8$ - $\text{CaMgSi}_2\text{O}_6$ system at high pressure.

ACKNOWLEDGMENTS

This research used resources of the National Energy Research Scientific Computing Center (NERSC), which is supported by the Office of Science of the U.S. Department of Energy under Contract No. DE-AC02-05CH11231. We also acknowledge NSF Grants ATM-0425059, EAR-0838182, EAR-0440057, EAR 09-48734, and DOE Grant DE-FG-03-91ER-14211.

REFERENCES CITED

- Asimow, P.D. and Ahrens, T.J. (2010) Shock compression of liquid silicates to 125 GPa: The anorthite-diopside join. *Journal of Geophysical Research*, 115, B10209, 28 pp.
- de Koker, N.P. (2010) Structure, thermodynamics, and diffusion in $\text{CaAl}_2\text{Si}_2\text{O}_8$ liquid from first-principles molecular dynamics. *Geochimica et Cosmochimica Acta*, 74, 5657–5671.
- de Koker, N.P., Stixrude, L., and Karki, B.B. (2008) Thermodynamics, structure, dynamics, and freezing of $\text{Mg}_2\text{Si}_4\text{O}_9$ liquid at high pressure. *Geochimica et Cosmochimica Acta*, 72, 1427–1441.
- Dunn, T. (1982) Oxygen chemical diffusion in three basaltic liquids at elevated temperatures and pressures. *Geochimica et Cosmochimica Acta*, 47, 1923–1930.
- Ghiorso, M.S. and Spera, F.J. (2009) Large Scale Simulations. In R. Wentzcovitch

- and L. Stixrude, Eds., *Theoretical and Computational Methods in Mineral Physics and Geophysics: Geophysical applications*, 71, p. 437–462. Reviews in Mineralogy and Geochemistry, Mineralogical Society of America and the Geochemical Society, Chantilly, Virginia.
- Ghiorso, M.S., Nevins, D., Cutler, I., and Spera, F.J. (2009) Molecular dynamics studies of CaAl₂Si₂O₈ liquid: Part II Equation of state and a thermodynamic model. *Geochimica et Cosmochimica Acta*, 73, 6937–6951.
- Ghiorso, M.S., Cutler, I., Nevins, D., and Spera, F.J. (2009) Molecular dynamics studies of CaAl₂Si₂O₈ liquid to 800 GPa: An equation of state, Hugoniot analysis, and thermodynamic model over the temperature range 2500–5000 K. American Geophysical Union, Fall Meeting 2009, abstract MR23B-01, San Francisco, California.
- Guillot, B. and Sator, N. (2007) A computer simulation study of natural silicate melts. Part I: low pressure properties. *Geochimica et Cosmochimica Acta*, 71, 1249–1265.
- Hofmann, A.W. and Magaritz, M. (1977) Diffusion of Ca, Sr, Ba, and Co in a basalt melt: Implications for the geochemistry of the mantle. *Geochimica et Cosmochimica Acta*, 42, 595–605.
- Jambon, A. and Carron, J.P. (1978) Étude expérimentale de la diffusion cationique dans une verre basaltique: alcalins et alcalinoterreux. *Bulletin de Mineralogie*, 101, 22–26.
- Karki, B.B. and Stixrude, L.P. (2010) Viscosity of MgSiO₃ liquid at Earth's mantle conditions: implications for an early magma ocean. *Science*, 328, 740–742.
- Karki, B.B., Bohara, B., and Stixrude, L. (2011) First-principles study of diffusion and viscosity of anorthite (CaAl₂Si₂O₈) liquid at high pressure. *American Mineralogist*, 96, 744–751.
- LaTourrette, T., Wasserburg, G.J., and Fahey, A.J. (1996) Self diffusion of Mg, Ca, Ba, Nd, Yb, Ti, Zr, and U in haplobasaltic melt. *Geochimica et Cosmochimica Acta*, 60, 1329–1340.
- Lacks, D.J., Rear, D.B., and van Orman, J.A. (2007) Molecular dynamics investigation of viscosity, chemical diffusivities and partial molar volumes of liquids along the MgO–SiO₂ join as functions of pressure. *Geochimica et Cosmochimica Acta*, 71, 1312–1323.
- Lesher, C.E., Hervig, R.L., and Tinker, D. (1996) Self diffusion of network formers (silicon and oxygen) in naturally occurring basaltic liquid. *Geochimica et Cosmochimica Acta*, 60, 405–413.
- Martin, G.B., Spera, F.J., Ghiorso, M.S., and Nevins, D. (2009) Structure, thermodynamic, and transport properties of molten Mg₂SiO₄: Molecular dynamics simulations and model EOS. *American Mineralogist*, 94, 693–703.
- Matsui, M. (1998) Computational modeling of crystals and liquids in the system Na₂O–CaO–MgO–Al₂O₃–SiO₂. In M.H. Manghnani and T. Yagi, Eds., *Properties of Earth and Planetary Materials at High Pressure and Temperature*, p. 145–148. Geological Monograph Series, American Geophysical Union, Washington, D.C.
- Metzler, R. and Klafter, J. (2004) The restaurant at the end of the random walk: Recent developments in the description of transport by fractional dynamics. *Journal of Physics A: Mathematical and General*, 37, R161–R208.
- Morgan, N.A. and Spera, F.J. (2001) A molecular dynamics study of the glass transition in CaAl₂Si₂O₈: Thermodynamics and tracer diffusion. *American Mineralogist*, 86, 915–926.
- (2001) The glass transition, structural relaxation and theories of viscosity: A molecular dynamics study of amorphous CaAl₂Si₂O₈. *Geochimica et Cosmochimica Acta*, 65, 4019–4041.
- Mungall, J.E. (2002) Empirical models relating viscosity and tracer diffusion in magmatic silicate melts. *Geochimica et Cosmochimica Acta*, 66, 125–143.
- Nevins, D. and Spera, F.J. (2007) Accurate computation of shear viscosity from equilibrium molecular dynamics simulations. *Molecular Simulation*, 33, 1261–1266.
- Nevins, D., Spera, F.J., and Ghiorso, M.S. (2009) Shear viscosity and diffusion in liquid MgSiO₃: Transport properties and implications for terrestrial planet magma oceans. *American Mineralogist*, 94, 975–980.
- Oganov, A.R., Brodholt, J.P., and Price, G.D. (2000) Comparative study of quasiharmonic lattice dynamics, molecular dynamics and Debye model in application to MgSiO₃ perovskite. *Physics of the Earth and Planetary Interiors*, 122, 277–288.
- Presnall, D.C., Gudfinnsson, G.H., and Walter, M.J. (2002) Generation of mid-ocean ridge basalts at pressures from 1 to 7 GPa. *Geochimica et Cosmochimica Acta*, 66, 2073–2090.
- Rapaport, D.C. (1995) *The Art of Molecular Dynamics Simulation*, 414 p. Cambridge University Press, U.K.
- Rigden, S.M., Ahrens, T. J., and Stolper, E.M. (1989) High-pressure equation of state of molten anorthite and diopside. *Journal of Geophysical Research*, 93(B1), 367–382.
- Rosenfeld, Y. and Tarazona, P. (1998) Density functional theory and the asymptotic high density expansion of the free energy of classical solids and fluids. *Molecular Physics*, 95, 141–150.
- Saika-Voivod, I., Soirotino, F., and Pool, P.H. (2000) Computer simulations of liquid silica: Equation of state and liquid–liquid phase transition. *Physical Review E*, 63, 011202.
- Spera, F., Nevins, D., Cutler, I., and Ghiorso, M. (2009) Structure, thermodynamic and transport properties of CaAl₂Si₂O₈ Liquid: Part I Molecular Dynamics simulations. *Geochimica et Cosmochimica Acta*, 73, 6937–6951.
- Spera, F., Ghiorso, M., and Nevins, D. (2011) Structure, transport, and thermodynamic properties of MgSiO₃: Comparison of molecular models and laboratory results. *Geochimica et Cosmochimica Acta*, 75, 1272–1296.
- Stevenson, J., Schmalian, J., and Wolynes, P. (2006) The shapes of cooperatively rearranging regions in glass-forming liquids. *Nature Physics*, 2, 268–274.
- Stixrude, L. and Karki, B.B. (2005) Structure and freezing of MgSiO₃ liquid in Earth's lower mantle. *Science*, 310, 297–299.
- Taniguchi, H. (1992) Entropy dependence of viscosity and the glass transition temperature of melts in the system diopside–anorthite. *Contributions to Mineralogy and Petrology*, 109, 295–303.
- Tinker, D., Lesher, C.E., and Hutcheon, I.D. (2003) Self-diffusion of Si and O in diopside anorthite melt at high pressures. *Geochimica et Cosmochimica Acta*, 67, 133–142.
- Udry, S., Bonfils, X., Delfosse, X., Forveille, T., Mayor, M., Perrier, C., Bouchy, F., Lovis, C., Pepe, F., Queloz, D., and Beraux, J.L. (2007) The HARPS search for southern extra-solar planets. XI. Super-Earths (5 and 8 M_⊕) in a 3-planet system. *Astronomy and Astrophysics*, Volume 469, May 6, 2007, 5p.
- Urbain, G., Bottinga, Y., and Richet, P. (1982) Viscosity of liquid silica, silicates and aluminosilicates. *Geochimica et Cosmochimica Acta*, 46, 1061–1072.
- Vinet, P., Ferrante, J., Smith, J.R., and Rose, J.H. (1986) A universal equation of state for solids. *Journal of Physics C: Solid State Physics*, 19, 1467–1473.
- Vuilleumier, R., Sator, N., and Guillot, B. (2009) Computer modeling of natural silicate melts: What can we learn from *ab initio* simulations. *Geochimica et Cosmochimica acta*, 73, 6313–6339.
- Wan, J.T.K., Duffy, T.S., Scandolo, S., and Car, R. (2007) First-principles study of density, viscosity, and diffusion coefficients of liquid MgSiO₃ at conditions of the Earth's deep mantle. *Journal of Geophysical Research*, 112, B03208. doi:10.1029/2005JB004135.
- Weeks, E. and Weitz, D. (2002) Subdiffusion and the cage effect studied near the colloidal glass transition. *Chemical Physics*, 284, 361–367.
- Zhang, Y., Ni, H., and Chen, Y. (2010) Diffusion data in silicate melts. In Y. Zhang and D. Cherniak, Eds., *Diffusion in Melts and Minerals*, 72, p. 311–408. Reviews in Mineralogy and Geochemistry, Mineralogical Society of America and the Geochemical Society, Chantilly, Virginia.

MANUSCRIPT RECEIVED APRIL 19, 2011

MANUSCRIPT ACCEPTED MARCH 13, 2012

MANUSCRIPT HANDLED BY BIJAYA KARKI